aerospace

MDPI

Article

A Time Cooperation Guidance for Multi-Hypersonic Vehicles Based on LSTM Network and Improved Artificial Potential Field Method

Jia Song *, Xiaowei Xu, Xindi Tong and Kai Zhao

School of Astronautics, Beihang University (BUAA), Beijing 100191, China
* Correspondence: songjia@buaa.edu.cn

Abstract: Time cooperation guidance is a key technology which can greatly increase the success rate of flight missions. However, it is difficult to satisfy all the strict constraints when designing the guidance system for multiple hypersonic vehicles. To solve these problems, a time cooperation framework is proposed. In this paper, the longitudinal predictor–corrector guidance law is firstly applied to meet the terminal and path constraints simultaneously. To settle the inaccurate estimation problem of residual flight time, a long short-term memory network (LSTM network) is trained and adopted in a time decision module, whose inputs are selected as six-dimensional feature vectors combined with the features of the sequential ballistics. In the time control module, the traditional artificial potential field method is modified to handle the no-fly zone constraints problem. Furthermore, the time potential field as a new type of potential field is added to indirectly control the flight time of hypersonic vehicles. The final simulation results show that the novel time potential field is compatible with the traditional potential field, which can satisfy the no-fly zone and flight time constraints at the same time. Meanwhile, compared with other time cooperative guidance, the algorithm proposed in this paper performs better in terms of time adjustable range.

Keywords: multi-hypersonic vehicles; multiple constraints condition; long short-term memory network (LSTM); artificial potential field (APF); time cooperative guidance

check for updates

Citation: Song, J.; Xu, X.; Tong, X.; Zhao, K. A Time Cooperation Guidance for Multi-Hypersonic Vehicles Based on LSTM Network and Improved Artificial Potential Field Method. *Aerospace* **2022**, *9*, 562. https://doi.org/10.3390/aerospace9100562

Academic Editor: Sergey Leonov

Received: 31 July 2022
Accepted: 14 September 2022
Published: 28 September 2022

Publisher's Note: MDPI stays neutral with regard to jurisdictional claims in published maps and institutional affiliations.

Copyright: © 2022 by the authors. Licensee MDPI, Basel, Switzerland. This article is an open access article distributed under the terms and conditions of the Creative Commons Attribution (CC BY) license (https://creativecommons.org/licenses/by/4.0/).

1. Introduction

With the modularization and stratification of anti-missile systems, the defensive objective is upgraded from the traditional ballistic missile to the hypersonic vehicle, which has stronger maneuverability. Therefore, the penetration ability of a single hypersonic vehicle is further compressed. By sharing information and complementing functions, multi-hypersonic vehicles can perform special tasks combined with cooperative strategies, which can greatly improve the efficiency of flight missions. In the face of enhanced defense systems, cooperative penetration consists of multiple vehicles with perfect robustness and concealment, which lead to the cooperation technology of multi-vehicles becoming the key factor of information warfare.

The cooperative penetration technology can effectively improve the threat level of hypersonic vehicles considered by anti-missile defense systems. However, the design process of cooperative guidance meets numerous constraints. The glide range of a hypersonic vehicle spans a wide scope of speed and airspace, which contains multiple harsh constraints like heat flow, overload, and dynamic pressure. Owing to the long range of the glide phase, there will be some blackout areas and no-fly zones which need to be avoided, which upgrades the difficulty of guidance law design. Furthermore, the control margin of flight time is required to be discussed as the ability to adjust the attack time or the attack angle in the cooperative flight mission. Hereby, the multiple constraint conditions and maneuverability of the hypersonic vehicle are necessary to consider in the design of the cooperative guidance law.

It is noted that time cooperation as one of the synergistic tasks indicates that the multi-vehicles arrive at the same target region at the coordinated time, which could enhance the effect of attack and increase the success rate of flight missions. The time cooperation guidance problem is formulated as the system shown in Figure 1: Suppose that there are multiple hypersonic vehicles in the task scenario, whose ranges of flight time turn out to be distinct due to the different conditions. The time cooperation guidance system requires finding the most suitable coordinate flight time among the flight ranges and guiding the multiple vehicles to the target region at uniform states. Moreover, the no-fly zones along the glide phase should be considered as well. As a result, there come to be multiple strict constraints that need to be solved.

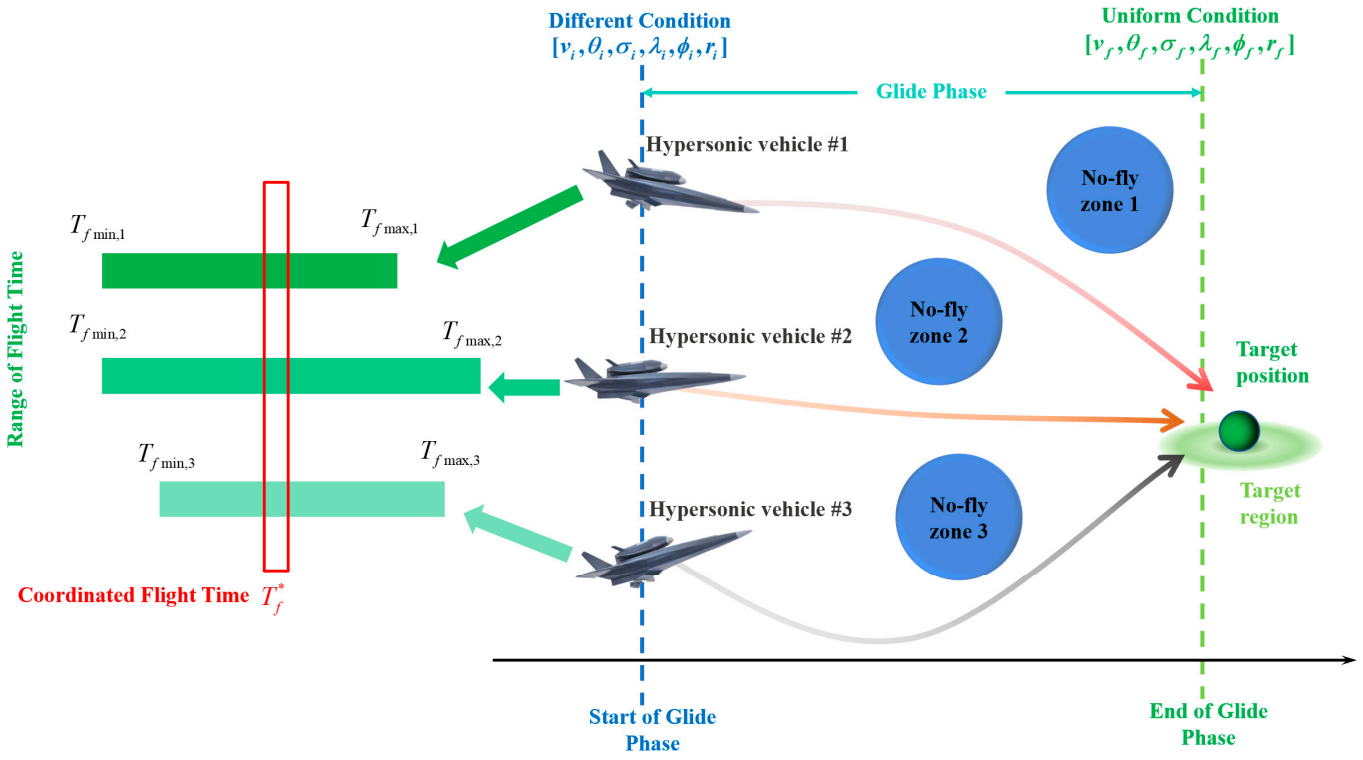

Figure 1. The schematic diagram of the time cooperative problem with hypersonic vehicles.

Due to the huge benefits of time cooperation, time cooperation technology has received worldwide attention from many studies [1–3]. Yu et al. [4] designed a two-stage strategy that the attack angle cooperation of multi-vehicles is realized in the first stage, and the attack time cooperation of multi-vehicles is achieved in the final stage. Li et al. [5] developed a time cooperation guidance that the residual flight time was roughly adjusted by the prediction of lateral guidance at first, and then the cooperative time was precisely controlled by longitudinal prediction-correction guidance to meet the time constraint. Although there has been some time-coordination guidance applied in hypersonic vehicle platforms, the time cooperation guidance mentioned above ignored the no-fly zone constraints in the glide phase. Yu et al. [6] proposed an analytic method that associates the residual flight time and flight range with the nominal trajectory deviation, and the bank angle reversal time was corrected to realize the time coordination and avoid the no-fly zones, but some assumptions about entry dynamics are unpractical. Li et al. [7] adopted the Gaussian pseudo-spectral method to realize the time coordination strategy of reusable launch vehicles (RLV) and satisfy the no-fly constraints at the same time. However, the computation cost of the pseudo-spectral method makes the algorithm hardly adopted online.

During the flight process without thrust, the state of hypersonic vehicles appears as time-varying, which contributes to the online requirement of time cooperative guidance. There is a further problem with estimating the residual time of vehicles, whose numerical

solution caused heavy computation while the analytical solution leads to unexpected, huge errors. Hereby, lots of studies have paid attention to real-time trajectory planning based on intelligent methods [8,9]. Chai et al. [10] built and trained a DNN network with a pre-generated trajectory that could drive a controller in real time and improve the reliability of path planning. Wang et al. [11] used the pseudo-spectral method to optimize the offline trajectory and then generate the optimal trajectory data. By training the parameters of DNN, the optimal neural network model was obtained to predict the guidance command. Moreover, with the wide application of reinforcement learning in various fields, many scholars try to adopt the DQN or DDPG methods to generate guidance instruction instead of traditional methods [12,13]. Zhao et al. [14] proposed a time cooperative guidance for quadrotors based on the DDPG method, which set the corresponding reward function in the training of DDPG. However, there is still rarely intelligent application on the time cooperation guidance design of multiple hypersonic vehicles.

Above all, there is a contradiction existing in no-fly zone avoidance, cooperation time constraints, and online planning requirements when designing the time cooperation guidance for multiple hypersonic vehicles. In this paper, a novel artificial potential field method (APF) combined with the LSTM network is developed to solve the multi-constraint conditions in time cooperation flight missions. The online LSTM network is to settle the unpredictable and uncontrollable issues of reentry flight time. By considering the characteristics of the high-speed and time-varying states in hypersonic vehicles as the input of the network, the LSTM network could have a strong generalization ability in predicting residual flight time. The APF method is developed in real-time by guidance design for the time cooperation problem, owing to its simplicity and lesser calculation burden. By introducing the new time potential field, the artificial potential method converts the time cooperation problems into lateral decision problems, which simplifies the time control and no-fly zone avoidance process. The major contribution of this work is successfully applying the LSTM network to the trajectory planning of multiple hypersonic vehicles and proposing a novel time potential field to solve the no-fly zones and coordinated time constraints in parallel.

The remaining paper is organized as follows. In Section 2, the 3DOF dynamic model of hypersonic vehicles and the multiple constraints described in the time cooperative problem are built, and the framework of time cooperation is also provided. Section 3 is the main part of this article, which details the implementation of the time cooperation framework based on the longitudinal predictor–corrector algorithm, the LSTM network, and the newly modified artificial potential field method. Section 4 displays the numerical simulation results to verify the feasibility of the proposed algorithm. Additionally, Section 5 finally draws the conclusion.

2. Formulation of Time Cooperation Problem

This section mainly describes the dynamic model of hypersonic vehicles and the multiple constraints during the glide phase.

2.1. Dynamic Model

Assuming the earth as a rotating sphere, the 3DOF dynamic model of hypersonic vehicles built in the semi-velocity coordinate system could be described as follows:

$$\begin{cases} \frac{dv_i}{dt} = -D_i + g'_{r_i}\sin\theta_i + C'_{v_i} \\ \frac{d\theta_i}{dt} = \frac{L_i\cos\gamma_i}{v_i} + \frac{g'_{r_i}\cos\theta_i}{v_i} + \frac{v_i\cos\theta_i}{r_i} + C'_{\theta_i} + C''_{\theta_i} \\ \frac{d\sigma_i}{dt} = \frac{L_i\sin\gamma_i}{v_i\cos\theta_i} + \frac{v_i\tan\phi_i\cos\theta_i\sin\sigma_i}{r_i\cos\theta_i} + C'_{\sigma_i} + C''_{\sigma_i} \\ \frac{d\lambda_i}{dt} = \frac{v_i\cos\theta_i\sin\sigma_i}{r_i\cos\phi_i} \\ \frac{d\phi_i}{dt} = \frac{v_i\cos\theta_i\cos\sigma_i}{r_i} \\ \frac{dr_i}{dt} = v_i\sin\theta_i \end{cases} \quad (1)$$

where the subscript i denotes the ith (i = 1, 2, ... , N) hypersonic vehicle, and N is the number of vehicles. θ_i and σ_i represent the flight path angle and heading angle, respectively, which decide the direction of the velocity v_i related to the ground. r_i is the distance between the vehicles and the center of the Earth. λ_i and ϕ_i stand for longitude and latitude. g'_{r_i} is the gravitational acceleration. γ_i is the bank angle which is the guidance instruction combined with the attack of angle α_i (AOA). C'_{v_i}, C'_{θ_i}, C''_{θ_i}, C'_{σ_i} and C''_{σ_i} are the additional items caused by Earth's rotation, which could be calculated as follows:

$$\begin{cases} C'_{v_i} = -\omega_e^2 r_i \left(\cos\phi_i \sin\phi_i \cos\sigma_i \cos\theta_i - \cos^2\phi_i \sin\theta_i\right) \\ C'_{\theta_i} = \frac{{\omega_e}^2 r_i}{v_i} \left(\cos\phi_i \sin\phi_i \cos\sigma_i \sin\theta_i + \cos^2\phi_i \cos\theta_i\right) \\ C''_{\theta_i} = 2\omega_e \cos\phi_i \sin\sigma_i \\ C'_{\sigma_i} = \frac{\omega_e^2 r_i \cos\phi_i \sin\phi_i \sin\sigma_i}{v_i \cos\theta_i} \\ C''_{\sigma_i} = -\frac{2\omega_e(\cos\phi_i \cos\sigma_i \sin\theta_i - \sin\phi_i \cos\theta_i)}{\cos\theta_i} \end{cases} \tag{2}$$

where ω_e is the Earth's angular velocity. D_i and L_i represent the aerodynamic drag and lift acceleration, which are given by

$$D_i = 0.5\rho(hi){v_i}^2 C_D(v_i, \alpha_i) S_{ref,i}/m_i \tag{3}$$

$$L_i = 0.5\rho(hi){v_i}^2 C_L(v_i, \alpha_i) S_{ref,i}/m_i \tag{4}$$

where ρ is the atmosphere density based on the 1976 US standard. $S_{ref,i}$ denotes the reference aerodynamic area of the vehicle, and m_i presents the mass of the vehicle. C_D and C_L represent the coefficient of drag and lift, which are fitted as the function of velocity and attack of angle.

2.2. Multiple Constraints during Glide Phase

It is noted that there are usually three general constraints described as heating rate, aerodynamic load, and dynamic pressure in the glide section. Moreover, the quasi-equilibrium gliding condition (QEGC) is adopted as a soft constraint to deduce the periodic oscillation. The four constraints belong to the path constraints which are given by:

$$\dot{Q}_i = k_Q \rho^{0.5} {v_i}^{3.15} \leq \dot{Q}_{\max,i} \tag{5}$$

$$n_i = \frac{1}{m_i g_0} \left| L_i \cos\alpha_i + D_i \sin\alpha_i \right| \leq n_{T_i,\max} \tag{6}$$

$$q_i = \frac{1}{2}\rho {v_i}^2 \leq q_{\max,i} \tag{7}$$

$$L_i \cos\gamma_{EQ,i} - \left(\frac{\mu_M}{{r_i}^2} - \frac{{v_i}^2}{r_i}\right) + 2\omega_e v_i \geq 0 \tag{8}$$

where Equations (5)–(7) present the heat flow, overload, and dynamic pressure separately, while Equation (8) is the QEGC condition. k_Q is the heating rate constant related to the structure of the vehicle. Additionally, the $\gamma_{EQ,i}$ stands for the bank angle of the QEGC under steady gliding. g_0 is the gravity acceleration and μ_M is the gravitational coefficient of the earth.

Besides the path constraints, the terminal constraints are necessary to be considered in normal flight missions, whose expression is detailed in:

$$\begin{cases} r\left(t_{f,i}\right) = r^*_{f,i}, v\left(t_{f,i}\right) = v^*_{f,i}, \\ \lambda\left(t_{f,i}\right) = \lambda^*_{f,i}, \phi\left(t_{f,i}\right) = \phi^*_{f,i} \end{cases} \tag{9}$$

where $t_{f,i}$ represent the arrival time of the ith vehicle. $r^*_{f,i}$ and $v^*_{f,i}$ denote the expected vehicle state about height and velocity, while $(\lambda^*_{f,i}, \phi^*_{f,i})$ represent the longitude and latitude position of the target. Equation (9) means that as long as the deviation of the terminal state $\delta h_{f,i}$, $\delta v_{f,i}$, and $s^*_{f,i}$ are within the tolerance value, the terminal constraints are met. $s^*_{f,i}$ is the terminal distance between the target and the vehicles.

Expect that the path and terminal constraints should be satisfied by each vehicle. The no-fly zone constraints are also important to avoid while executing the penetration mission. By modeling the no-fly zone as a cylindrical region with infinite height, the no-fly zone constraints are converted into geographical constraints, which are given by:

$$(\lambda_i - \lambda_c)^2 + (\phi_i - \phi_c)^2 \geq R_c^2 / r_i^2 \tag{10}$$

where λ_c and ϕ_c are the positions of the centers of the no-fly zones. Additionally, R_c represents the radius of the no-fly zones.

In this paper, the main constraint of the glide phase is the coordinate time constraint for multiple vehicles' flight missions, which is depicted as:

$$t_{f,1} = t_{f,2} = \ldots = t_{f,N} = T^*_f \tag{11}$$

where T^*_f is the coordinate time generated by the information exchange of multiple vehicles. The effect of time cooperative guidance is to produce the command sequence $[\alpha_i, \gamma_i]$ for each vehicle, whose glide path can meet the total constraints as Equations (5)–(11) so that the cooperative mission could be accomplished.

2.3. The Framework of Time Cooperative Guidance

In this paper, the framework of the time cooperative guidance device is to solve the cooperation problem under multi-constraints and is shown in Figure 2. The guidance framework is divided into double-layer modules with a time prediction solver. A solver of residual time prediction-based LSTM network is designed for estimating the time-to-go function, which can greatly save the time of computation about the vehicle's residual flight time while guaranteeing accuracy. The up-layer module is called the cooperative time decision module, which collects the states of vehicles and multiple constraints, and then interacts with the time solver to obtain the flight time ranges of multi-vehicles and determine the coordinated flight time T^*_f. The down layer, as named as the cooperative time control module, is applied to receive the T^*_f and control the current flight time T^i_f close to the coordinated time T^*_f based on the time potential field proposed in this paper. These three parts are mutually communicated with each other to realize the function of time cooperation, whose implementation will be detailed in the following sections.

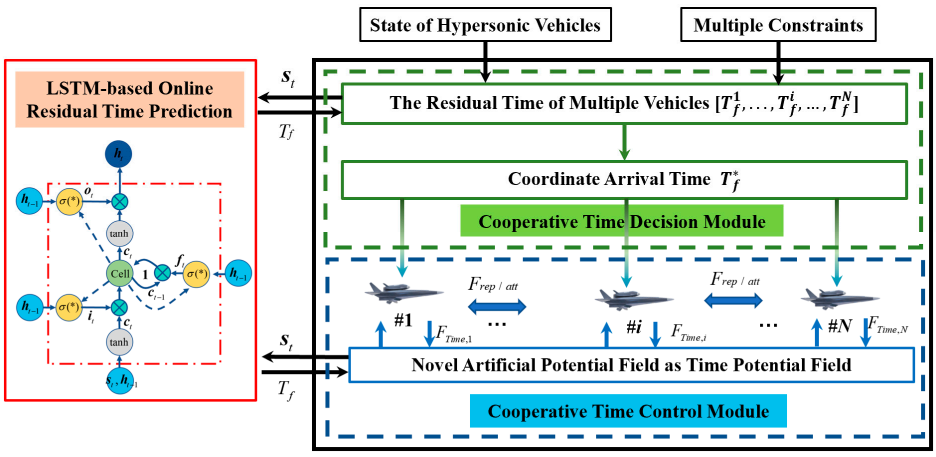

Figure 2. The framework of time cooperative guidance.

3. Time Cooperative Guidance Design

3.1. Predictor–Corrector Algorithm for Longitudinal Guidance

Section 2.2 shows that the trajectory planning of the glide phase is a hardly restricted problem. Before settling the time coordination constraint, it is significant to resolve the path and terminal constraints in a single vehicle. Thus, a predictor–corrector algorithm is proposed in longitudinal guidance.

The core process of the predictor–corrector algorithm is the prediction of the terminal state and the correction of the guidance commands according to the predicted result. To meet the terminal height and velocity constraints at the same time, we define the normalized energy e_i as $e_i = \mu_M/r_i - v_i^2/2$, where r_i and v_i are the flight states related to the vehicle. Therefore, the equation (9) is converted to

$$\begin{cases} s_{f,i} = s\left(e_{f,i}\right) = 0 \\ e_{f,i} = \frac{\mu_M}{r_{f,i}} - \frac{v_{f,i}^2}{2} \end{cases} \tag{12}$$

From the dynamic model Equation (1) and by deviating the normalized energy e_i and range-to-go s_i, the relationship between e_i and the range-to-go s_i could be inferred as:

$$\frac{ds_i}{dt_i} = v_i \cos\theta_i, \frac{de_i}{dt_i} = -\dot{v}_i v_i = -D_i v_i \Rightarrow \frac{ds_i}{de_i} = -\frac{\cos\theta_i}{D_i} \tag{13}$$

where s_i denotes the longitudinal distance between vehicle and target, which could be calculated as $s_i = R_0 \cdot \arccos\left[\sin\phi i \sin\phi f, i + \cos\phi i \cos\phi f, i \cos\left(\lambda_{f,i} - \lambda_i\right)\right]$, and R_0 is the radius of Earth.

To simplify the guidance process, by pre-designing the profile of the AOA, the prediction process of longitudinal motion is integrating Equation (13) on the interval $[e_{0,i}, e_{f,i}]$ with a pre-set AOA, where $e_{0,i}$ and $e_{f,i}$ stand for the initial energy and the expected terminal energy. As the AOA of the current guidance period is determined, the corrector process searches the optimal bank angle command γ_i^* to let the integer result close to the expected value, which is usually solved by the secant method as:

$$\begin{aligned} &F_i(\gamma_i) = s_i(\gamma_i) - s_i^* \\ &|\gamma_i|^{k+1} = |\gamma_i|^k - \frac{F_i^k}{F_i^k - F_i^{k-1}}\left(|\gamma_i|^k - |\gamma_i|^{k-1}\right) \end{aligned} \tag{14}$$

where k is the count of iteration. Through the predictor–corrector process, the γ_i is updated to the optimum value γ_i^*, which meets the terminal constraints. By introducing the calculation formulation of atmosphere density $\rho_i = \rho_0 e^{-\beta h_i}$, Equations (5)–(7) convert to height constraints versus velocity, which can limit the amplitude of the bank angle combined with Equation (8) given by:

$$\left.\begin{aligned} |\gamma_{Q,i}(v_i)| &\leqslant \cos^{-1}\left[\left(g - \frac{{v_i}^2}{r_i}\right)\frac{2m_i {v_i}^{4.3}}{C_{L,i}S_{ref,i}}\left(\frac{k_Q}{\dot{Q}_{\max,i}}\right)^2\right] = |\gamma_{Q\max,i}(v_i)| \\ |\gamma_{n,i}(v_i)| &\leqslant \cos^{-1}\left[\left(g - \frac{{v_i}^2}{r_i}\right)\frac{\sqrt{1+\left(C_{D,i}/C_{L,i}\right)^2}}{g_0 n_{\max,i}}\right] = |\gamma_{n\max,i}(v_i)| \\ |\gamma_{q,i}(v_i)| &\leqslant \cos^{-1}\left[\left(g - \frac{{v_i}^2}{r_i}\right)\frac{m}{C_{L,i}q_{\max,i}S_{ref,i}}\right] = |\gamma_{q\max,i}(v_i)| \end{aligned}\right\} \tag{15}$$

where β is a constant value as $1/7200$. $|\gamma_{Q\max,i}(v_i)|$,$|\gamma_{n\max,i}(v_i)|$, and $|\gamma_{q\max,i}(v_i)|$ represent the maximum absolute value of the bank angle under the maximum heating rate $\dot{Q}_{\max,i}$, overload $n_{\max,i}$, and dynamic pressure $q_{\max,i}$. To further correct the bank angle command,

the compensation based on the height feedback is designed to suppress the oscillate ballistic. Therefore, the absolute amplitude of the bank angle in the glide phase is expressed as:

$$\begin{aligned} \left|\gamma^*_{cmd,i}\right| &= \left|\gamma^*_i\right| + K_{hp,i}(h_{QEGC,i} - h_i) + K_{hd,i}(\dot{h}_{QEGC,i} - \dot{h}_i) \\ \left|\gamma^*_{c,i}(v_i)\right| &= \min\left\{\left|\gamma^*_{cmd,i}(v_i)\right|, \left|\gamma_{Q\max,i}(v_i)\right|, \left|\gamma_{n\max,i}(v_i)\right|, \left|\gamma_{q\max,i}(v_i)\right|\right\} \end{aligned} \tag{16}$$

where $\left|\gamma^*_{cmd,i}\right|$ is the command bank angle feedback by height, and $\left|\gamma^*_{c,i}(v_i)\right|$ is the final bank angle limited by the path constraints. $h_{QEGC,i}$ and $\dot{h}_{QEGC,i}$ denote the height and the deviation of the height under the QEGC condition. $K_{hp,i}$ and $K_{hd,i}$ are the feedback coefficients which are built as a type of PD control for trajectory planning.

As the predictor–corrector algorithm has generated the absolute amplitude of the bank angle which satisfied the path and terminal constraints concurrently, the sign of the bank angle will be determined by the heading error corridor in the traditional lateral method [15,16]. The sketch of the heading error corridor is shown in Figure 3.

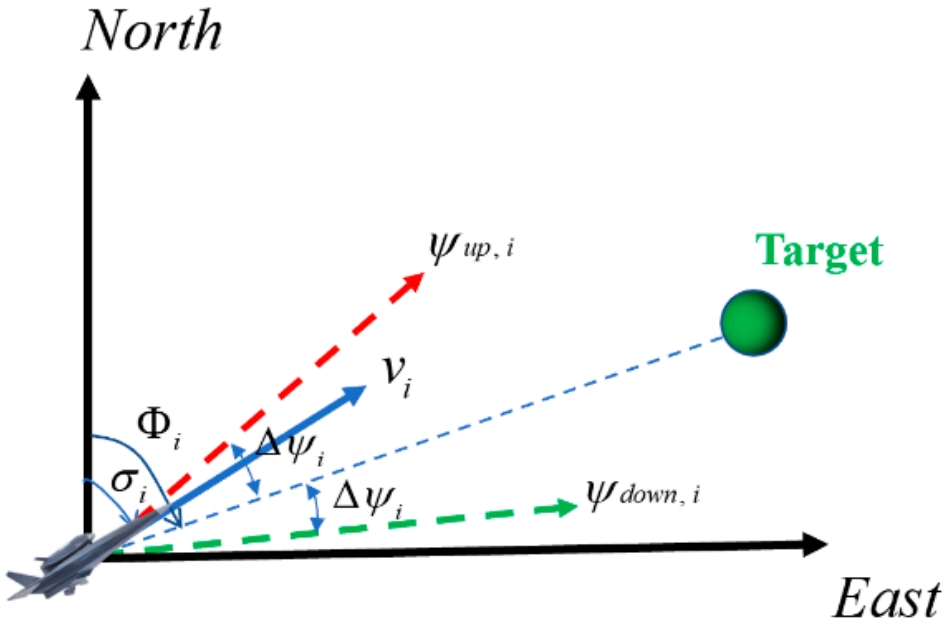

Figure 3. The sketch of heading error corridor.

As shown in Figure 3, the heading error corridor consists of the up-heading angle $\psi_{up,i}$ and the down-heading angle $\psi_{down,i}$, which are determined by the sight line of the target and corridor width $\Delta\psi_i$. Additionally, the sign of the bank angle is defined by the heading error $\Delta\sigma_i$, given by:

$$\begin{aligned} \Phi_i &= \arctan\left[\frac{\sin(\lambda_{f,i} - \lambda_i)}{\cos\phi_i \tan\phi_{f,i} - \sin\phi_i \cos(\lambda_{f,i} - \lambda_i)}\right] \\ \Delta\sigma_i &= \sigma_i - \Phi_i \end{aligned} \tag{17}$$

where Φ_i is the line-of-sight angle to target and $\Delta\sigma_i$ is the heading error. Due to the coordinate time constraints, the traditional lateral method fails to meet the requirement. As a result, a newly lateral method based on the artificial potential field is developed to satisfy the time constraint which is described in Section 3.3.

3.2. Cooperative Time Decision Based on LSTM Network

Before introducing the lateral guidance, it is the foundation of time cooperation to solve the estimation problem about the time-to-go. Due to the time-varying state of vehicles during the glide phase, it is difficult to accurately predict the residual flight time. There

are normally two solutions: the numerical solution [16] is accuracy but occupies large computation, while the analytical solution [17–19] is faster but lacks precision. Thus, a cooperative time decision module based on the LSTM network is built to overcome the contradiction between accuracy and the calculation efficiency.

As a variant of a recurrent neural network, the LSTM network has a better performance in its prediction function compared to traditional neural networks like DNN. By the special construction of the input gate, output gate, and forge gate, the regular operation of the network of read, write, and reset could be executed in the inner cell unit. The typical forward calculation process is given by:

$$\begin{cases} \boldsymbol{f}_t = \sigma\left(\boldsymbol{b}_f + \boldsymbol{W}_f \boldsymbol{s}_t + \boldsymbol{U}_f \boldsymbol{h}_{t-1}\right) \\ \boldsymbol{i}_t = \sigma(\boldsymbol{b}_i + \boldsymbol{W}_i \boldsymbol{s}_t + \boldsymbol{U}_i \boldsymbol{h}_{t-1}) \\ \boldsymbol{o}_t = \sigma(\boldsymbol{b}_\circ + \boldsymbol{W}_o \boldsymbol{s}_t + \boldsymbol{U}_o \boldsymbol{h}_{t-1}) \\ \boldsymbol{c}_t = \tanh(\boldsymbol{b}_c + \boldsymbol{W}_c \boldsymbol{s}_t + \boldsymbol{U}_c \boldsymbol{h}_{t-1}) \\ \boldsymbol{l}_t = \boldsymbol{f}_t \boldsymbol{l}_{t-1} + \boldsymbol{i}_t \boldsymbol{c}_t \\ \boldsymbol{h}_t = \boldsymbol{o}_t \tanh \boldsymbol{l}_t \end{cases} \tag{18}$$

where subscript t is the current time and $t-1$ is the last time. $\boldsymbol{s}_t$ denotes the input vector of LSTM. $\boldsymbol{c}_t$ and $\boldsymbol{l}_t$ represent the candidate values and new values of memory units. $\boldsymbol{f}_t$, $\boldsymbol{i}_t$, and $\boldsymbol{o}_t$ stand for the forge gate, input gate, and output gate, whose untrained input weight matrix, regression weight matrix, and bias vector are marked as $\boldsymbol{W}$, $\boldsymbol{U}$, and $\boldsymbol{b}$, respectively. $\boldsymbol{h}_t$ is the output of LSTM's hidden layer, whose dimensions are determined by the number of nodes. σ and tanh are the nonlinear functions that denote the sigmoid and hyperbolic tangent active functions.

Though the ballistic is a time sequence, the input vector based on the predictor–corrector algorithm is chosen as:

$$s_t = \left[r, V_{LOS}, S_{res}, \Delta\psi_{BW}, \gamma, \dot{L}_{cross}\right]^T \tag{19}$$

where r is the geocentric distance, and V_{LOS} is the line-of-sight velocity, which can be calculated as $V_{LOS} = v \times \cos(\Delta\psi)$. S_{res} stands for the range-to-go of vehicles. $\Delta\psi_{BW}$ is the width of the heading error corridor, which is obtained by $\Delta\psi_{BW} = \psi_{up} - \psi_{down}$. γ is the current bank angle. $\dot{L}_{cross}$ is the deviation of the cross range, which can be inferred from $\dot{L}_{cross} = R_0 v \sin\theta/(R_0 + h)$. The r, V_{LOS}, and S_{res} are chosen as the longitudinal variables, and the $\Delta\psi_{BW}$, γ, and $\dot{L}_{cross}$ are applied as the lateral control quantity and observed quantity. The longitudinal and lateral variables are both used to improve the network accuracy of the LSTM network.

After the simulation of the predictor–corrector guidance, the label of the network T_f can be inferred by pushing back the flight time. The training process of the p-code is detailed below.

Algorithm 1: Residual Flight Time Prediction

randomly generate 4000 ballistic paths by the prediction—correction guidance law and set up data buffering $\Re$
initial LSTM network weight value $\boldsymbol{W}$, $\boldsymbol{U}$, and $\boldsymbol{B}$
set $lr, n\_epoch, batch\_size, random\_seed, patience, timestep$
for $epoch = 1, n\_epoch$ do
    for $batch\_size = 1, n\_batch\_sizes$ do
        obtain the ballistic data $[s_t, T_f]$
            $net\_in = [r, V_{LOS}, S_{res}, \Delta\psi_{BW}, \gamma, \dot{L}_{cross}]$, $net\_out = [T_f]$ data feature excludes abnormal and normalization
        update LSTM network parameters by using the Adam algorithm: $loss = \frac{1}{mn}\sum_{j}^{m}\sum_{i=1}^{n}\left[f\left(x_{ij}\right) - y_{ij}\right]^2$
end for

As described in the p-code, *lr* is the learning rate of LSTM, and *n_epoch* is the iteration times of training, while *batch_size* is the number of training data for each epoch. *random_seed*,*timestep*, and *patience* are the coefficients of LSTM related to training loss. The m and n in the loss function denote the number of ballistic and sample points in each ballistic. By continuously updating the weight value $\boldsymbol{W}$, $\boldsymbol{U}$, and $\boldsymbol{b}$, the whole process of training LSTM will end until the loss declines to the expected value, which means the trained LSTM network could be adopted to predict the residual flight time.

By introducing the trained LSTM network, the time prediction problem is converted into a mapping relation between the current state s_t and T_f. In the simulation, we found that the residual time is a positive correlation with $\Delta\psi_{BW}$, which could predict the flight time range as follows.

$$\begin{aligned} T_{f\min,i} &= F(\Delta\psi_{\min,i}) \\ T_{f\max,i} &= F(\Delta\psi_{\max,i}) \end{aligned} \tag{20}$$

where $F(*)$ stands for the mapping function based on the trained LSTM. $[T_{f\min,i}, T_{f\max,i}]$ is the flight time range of the ith vehicle. By collecting the whole flight ranges of multiple vehicles, the coordinate time could be calculated as:

$$T_f^* = \frac{\max\left\{T_{f\min,1},\ldots,T_{f\min,i},\ldots,T_{f\min,N}\right\} + \min\left\{T_{f\max,1},\ldots,T_{f\max,i},\ldots,T_{f\max,N}\right\}}{2} \tag{21}$$

where T_f^* is the coordinated time constraint, which is delivered to each vehicle by the cooperative time decision module.

3.3. Cooperative Time Control Based on Time Potential Field

After building the basics of time cooperation, we will handle the rest of the constraint conditions including the no-fly zones and time constraints in this part. To approach the target with a small heading error, the reference heading angle of traditional lateral guidance is generally taken as the sight angle from vehicle to target, which is inapplicable to deal with the no-fly zone and coordinated time constraints. Therefore, an improved lateral guidance-based artificial potential field (APF) [20] is designed for satisfying both of the constraints by transforming the problem into the reference heading angle decision problem.

The typical APF method consists of an attraction and repulsion potential field, where the vehicle will be subjected to the attractive force and repulsive force in the composite potential field. In articles [21,22], the scholars set the direction of virtual resultant force as the reference heading angle. The idea of this paper is similar to the previous works, but the form of both potential fields is different. Moreover, the biggest difference is that a new time potential field is added.

Considering the limited maneuver capacity of hypersonic vehicles, the forms of the attractive potential field and repulsive potential field are designed as:

$$U_{att}(\mathbf{d}_i) = \frac{1}{2}K_{att}e^{-\|\mathbf{d}_i-\mathbf{d}_{f,i}\|^2} \tag{22}$$

$$U_{rep}^j(\mathbf{d}_i) = \begin{cases} K_\infty, & \|\mathbf{d}_i-\mathbf{d}_{nz,j}\| < R_{nz,j}, \lambda_i \le \lambda_{nz,j} \\ \frac{K_{rep}}{2}\left(\frac{1}{\|\mathbf{d}_i-\mathbf{d}_{nz,j}\|}-\frac{1}{\rho_{nz,j}}\right)^2\|\mathbf{d}_i-\mathbf{d}_{f,i}\|^4, & R_{nz,j} \le \|\mathbf{d}_i-\mathbf{d}_{nz,j}\| \le \rho_{nz,j}, \lambda_i \le \lambda_{nz,j} \\ 0, & \text{otherwise} \end{cases} \tag{23}$$

where K_{att} and K_{rep} represent the coefficients of the attention and repulsion potential fields, respectively. K_∞ is an infinite constant. $\mathbf{d}_i = [\lambda_i, \phi_i]^T$,$\mathbf{d}_{f,i} = \left[\lambda_{f,i}, \phi_{f,i}\right]^T$, and $\mathbf{d}_{nz,j} = [\lambda nz, j, \phi nz, j]^T$ stand for the geographical positions of the ith vehicle, target, and the center position of the jth ($j = 1, 2, \ldots, M$) no-fly zone, and M is the number of no-fly zones. Additionally, the operator $\|*\|$ calculates the spherical trigonometry between two

positions. $R_{nz,j}$ is the radius of the no-fly zone, and $\rho_{nz,j}$ is the influence radius. The influence radius enlarges the real radius of no-fly zones, which can require an earlier maneuver before flying into it. The type of attractive potential is designed as an exponential form, which solved the unreachable problem.

The potential field forces can be inferred from the negative gradient of the potential fields, which are given as:

$$\mathbf{F}_{att}(\mathbf{d}_i) = -\nabla U_{att}(\mathbf{d}_i) = \frac{1}{2}\|\mathbf{d}_i - \mathbf{d}_{f,i}\| K_{att} e^{-\|\mathbf{d}_i - \mathbf{d}_{f,i}\|^2} \mathbf{n}_{att,i} \tag{24}$$

$$\mathbf{F}^j_{rep}(\mathbf{d}_i) = -\nabla U^j_{rep}(\mathbf{d}_i) = \begin{cases} K_\infty, & \|\mathbf{d}_i - \mathbf{d}_{nz,j}\| < R_{nz,j}, \lambda_i \le \lambda_{nz,j} \\ F^j_{rep1}\mathbf{n}^j_{nz,i} + F^j_{rep2}\mathbf{n}^j_{g,i}, & R_{nz,j} \le \|\mathbf{d}_i - \mathbf{d}_{nz,j}\| \le \rho_{nz,j}, \lambda_i \le \lambda_{nz,j} \\ 0, & \text{otherwise} \end{cases} \tag{25}$$

where $\mathbf{n}_{att,i}$ is the unit direction vector of attentive force which points to the target. $\mathbf{n}^j_{nz,i}$ and $\mathbf{n}^j_{g,i}$ are the unit direction vectors of F^j_{rep1} and F^j_{rep2} which denote the two repulsive forces received in the repulsion potential field, which are calculated as:

$$F^j_{rep1} = \frac{K_{rep}}{2}\left(\frac{1}{\|\mathbf{d}_i - \mathbf{d}_{nz,j}\|} - \frac{1}{\rho_{nz,j}}\right)\frac{\|\mathbf{d}_i - \mathbf{d}_{f,i}\|^4}{\|\mathbf{d}_i - \mathbf{d}_{nz,j}\|^2} \tag{26}$$

$$F^j_{rep2} = K_{rep}\left(\frac{1}{\|\mathbf{d}_i - \mathbf{d}_{nz,j}\|} - \frac{1}{\rho_{nz,j}}\right)^2 \|\mathbf{d}_i - \mathbf{d}_{f,i}\|^3 \tag{27}$$

The direction of the unit vector $\mathbf{n}^j_{nz,i}$ is orthogonal to the line-of-sight of the jth no-fly zone, which points to the direction far from the center of the no-fly zone so that the vehicle could fly away. The direction of $\mathbf{n}^j_{g,i}$ is the same as $\mathbf{n}_{att,i}$. The F^j_{rep2} occupies the majority part of the repulsive force, which enhances the attentive force while approaching the target and prevents the vehicle stuck in the local minimum.

As the typical potential has been designed to satisfy the no-fly zone constraints, the novel time potential field is built to meet the time control functions. It is easy to figure out that the more the cross error of the trajectory relative to the sight-line of the target, the more flight time the vehicle takes, and the opposite conclusion will be inferred from the contrary condition. Therefore, a time potential field is developed to control the cross error of vehicles, which is expressed as:

$$U_{Time}(\mathbf{d}_i) = \frac{1}{2}K_t\left|T^*_f - T_{f,i}\right|^2 \tag{28}$$

where K_t is the time coefficient. It is noted that the numeric value of the time potential field is associated with the time error caused by the current residual flight time $T_{f,i}$ and coordinated time T^*_f regardless of the distance information. The time potential force is calculated as:

$$\mathbf{F}_{Time}(\mathbf{d}_i) = -\nabla U_{Time}(\mathbf{d}_i) = K_t\left|T^*_f - T_{f,i}\right|\mathbf{n}_{T,i} \tag{29}$$

where $\mathbf{n}_{T,i}$ is the unit direction vector of the time potential force $\mathbf{F}_{Time}$. The direction of $\mathbf{n}_{T,i}$ is orthogonal to the line-of-sight of the target, which can be expressed as $\mathbf{n}_{T,i} = [\sin\varphi_{t,i}, \cos\varphi_{t,i}]^T$. The calculation method of angle $\varphi_{t,i}$ is given by:

$$\varphi_{t,i} = \begin{cases} \operatorname{atan}\left[\dfrac{\sin(\lambda_{f,i}-\lambda_i)}{\cos\phi_i \tan\phi_{f,i} - \sin\phi_i \cos(\lambda_{f,i}-\lambda_i)}\right] + \dfrac{\pi}{2}, \\ (T_f^* > T_{f,i} \text{ and } \sigma_i > \Phi_i) \text{ or } (T_f^* < T_{f,i} \text{ and } \sigma_i < \Phi_i) \\ \operatorname{atan}\left[\dfrac{\sin(\lambda_{f,i}-\lambda_i)}{\cos\phi_i \tan\phi_{f,i} - \sin\phi_i \cos(\lambda_{f,i}-\lambda_i)}\right] - \dfrac{\pi}{2}, \\ (T_f^* > T_{f,i} \text{ and } \sigma_i > \Phi_i) \text{ or } (T_f^* < T_{f,i} \text{ and } \sigma_i > \Phi_i) \end{cases} \tag{30}$$

Equation (30) mainly describes the direction of the time potential force. The effect of the time potential force is visually displayed in Figure 4

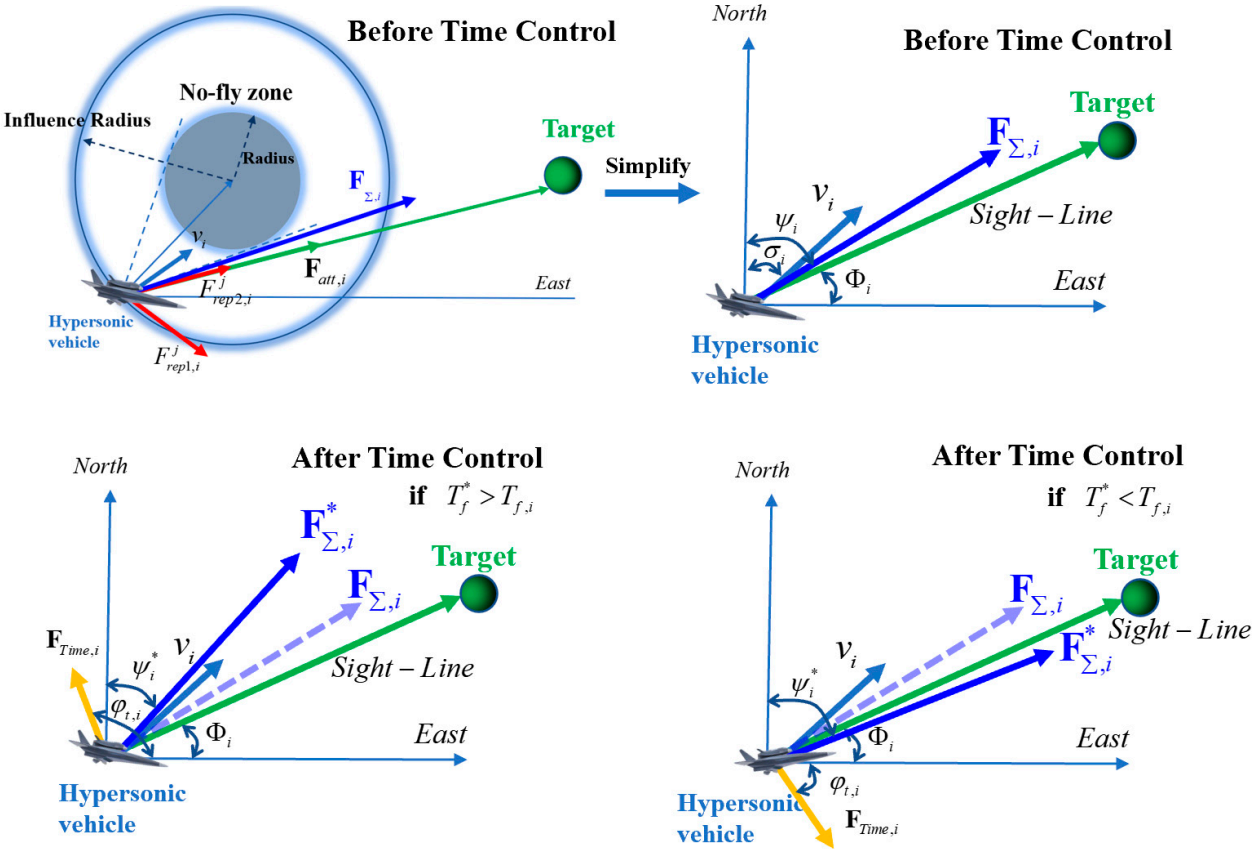

Figure 4. The multiple virtual forces received by the hypersonic vehicle in the artificial potential field.

As can be seen in Figure 4, the analysis process of the multiple virtual forces received in the artificial potential field is divided into two phases. Before the time control phase, the vehicle receives attentive and repulsive forces under the influence of the no-fly zone, which are consistent with the resultant force $\mathbf{F}_{\Sigma,i}$. In the time control phase, the time potential field would be adopted, and the direction of the force is decided by the time error. After the time control, the vehicle would be closer to or further from the sight-line by the effect of the modified resultant $\mathbf{F}^*_{\Sigma,i}$, which is given by:

$$\begin{aligned} \mathbf{F}^*_{\Sigma,i}(\mathbf{d}_i) &= \mathbf{F}_{att}(\mathbf{d}_i) + \sum_{j=1}^{M} \mathbf{F}^j_{rep}(\mathbf{d}_i) + \mathbf{F}_{Time}(\mathbf{d}_i) \\ \psi_i^* &= \angle \mathbf{F}^*_{\Sigma,i}(\mathbf{d}_i) \end{aligned} \tag{31}$$

where ψ_i^* is the reference heading angle for the ith vehicle. The reference heading angle ψ_i^* will be used to replace the traditional one, and the new heading angle corridor can determine the symbol of the bank angle, which is expressed as:

$$\begin{aligned} \text{sign}(\gamma_i^t) &= \begin{cases} -1 & \sigma_i \geq \psi_{up,i} \\ 1 & \sigma_i \leq \psi_{down,i} \\ \text{sign}\left(\gamma_i^{t-1}\right) & \text{otherwise} \end{cases} \\ \psi_{up,i} &= \min[\psi_{upLimit,i}, \psi_i^* + \Delta\psi_i]; \\ \psi_{down,i} &= \max[\psi_{\text{down}Limit,i}, \psi_i^* - \Delta\psi_i]; \end{aligned} \tag{32}$$

where $\Delta\psi_i$ is a pre-design value about the width of the corridor. $\psi upLimit, i$ and $\psi \text{down}Limit, i$ are the heading directions of the tangent line from the vehicle to the circle of the no-fly zone. It is noted that, because the priority of avoiding the no-fly zone is higher than the time cooperation, the up-heading angle $\psi_{up,i}$ and the down-heading angle $\psi_{down,i}$ are further limited.

Equations (31) and (32) define the magnitude and direction of the artificial potential resultant, and the attractive force takes the major component in the virtual resultant, while the repulsive forces and time potential force settle to adjust the direction of the attractive force, which changes the reference heading angle indirectly. Therefore, there will always be a non-zero resultant and guidance of the lateral actions of vehicles, which avoids the local minimum problem usually occurring in the traditional artificial potential field.

With the complement of lateral guidance, the flow chart of time cooperation guidance is shown in Figure 5.

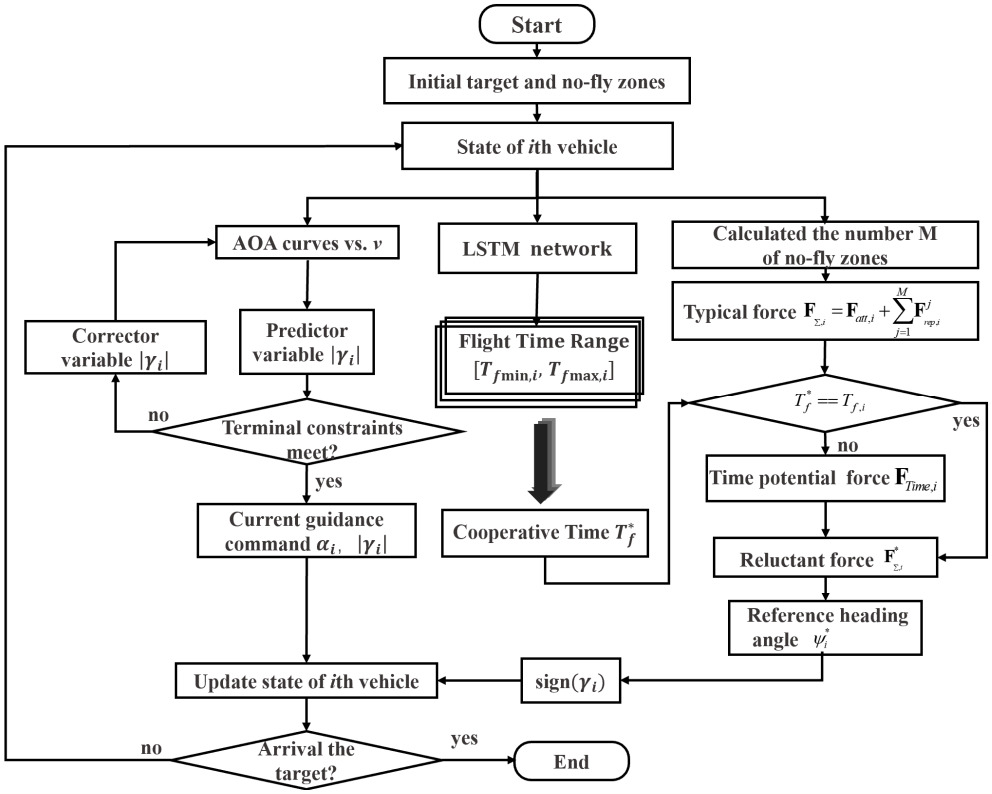

Figure 5. The flow chart of time cooperation guidance.

As shown in Figure 5, the start of the time cooperation guidance law is to initialize the multi-constraints and states of the vehicles. Additionally, the longitudinal guidance command $[\alpha_i, |\gamma_i|]$ is then generated by the predictor–corrector algorithm, which satisfies the constraints (5)–(9). Collaterally, the cooperative time is calculated by the time decision

module based on the LSTM network and transmits the T_f^* to each vehicle. At the same time, the reluctant force $\mathbf{F}_{\sum,i}^*$ is computed in the composite artificial potential field combined with the cooperative time, which meets the rest of the constraints (10) and (11). When all of the vehicles have arrived at the expected target position, the process of time cooperation guidance comes to end.

4. Simulation Results

The research object of this paper is CAV-H, which is a ratio near-space reentry vehicle with high L/D. The detailed dates of CAV-H are set as $m_{\mathrm{CAV-H}} = 907$ kg and $S_{ref} = 0.48$ m^2. The path constraints are set as: the maximum heating rate is set as $\dot{Q}_{\max,i} = 1000$ KW/m^2, the maximum overload is $n_{\max,i} = 6$ g, and the maximum dynamic pressure is $q_{\max,i} = 300$ kPas. The terminal state constraints are set as $h_{f,i}^* = 25$ km, $\delta h_{f,i} = 2.5$ km, $v_{f,i}^* = 1550$ m/s, and $\delta v_{f,i} = 20$ m/s. The center of the target region is set as $[\lambda_{f,i}^*, \phi_{f,i}^*] = [55^{\circ}\mathrm{E}, 5.5^{\circ}\mathrm{N}]$, the final range-to-go is set as $s_{f,i}^* = 100$ km, and the message of the target region is pre-set before emission. On the demand of time cooperation, the multiple hypersonic vehicles need to achieve the target region at the coordinated time.

The algorithm is conducted on a PC with an Intel Core i5-8400 processor and 16.0 GB memory and the Windows operating system. The simulation software is MATLAB R2018a.

4.1. Generation of the Dataset

The dataset consisting of 4000 ballistics is generated by the predictor–corrector algorithm, whose simulation initial conditions are given in Table 1.

Table 1. Simulation initial conditions for generating dataset.

Parameters	Value Range
Initial height h_0	65–75 km
Initial velocity v_0	6500–7500 m/s
Initial path angle θ_0	−5–5°
Initial heading angle σ_0	80–90°
Corridor width $\Delta\psi_i$	2–20°
Initial longitude and latitude [λ_0,ϕ_0]	(−20° E–20° E), (−20° N–20° N)
Terminal longitude and latitude [λ_f,ϕ_f]	(60° E–70° E), (−5° N–5° N)

By randomly producing the initial state of the vehicle, the ballistics samples are generated until the number of simulation times reaches 4000. Additionally, the statistics of the flight time are shown in Figure 6.

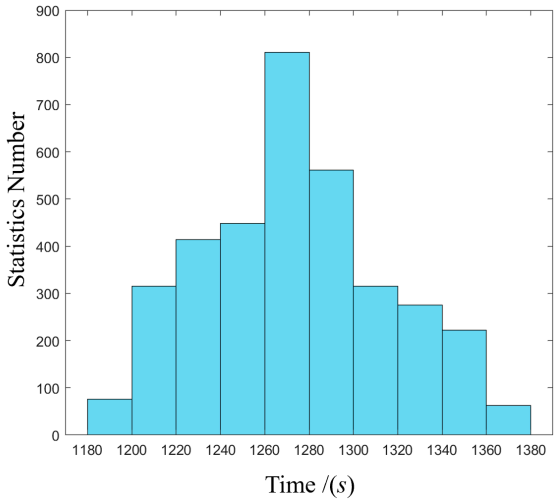

Figure 6. The statistics of flight time.

As shown in Figure 5, since the simulation program was carried out with the predictor–corrector algorithm without adding the modified artificial potential field method, the range of flight time is similar to the Gaussian distribution with an error of about ±100 s under different initial simulation conditions. Therefore, the main function of the time cooperative guidance is to narrow the flight time error, which can ensure the coordinated arrival time of multiple vehicles with different states.

The 4000 ballistics generated above were integrated into the dataset of the LSTM network. Considering that there are approximately 12,000 sampling points on each ballistic, the overall magnitude of the dataset is around 20 million. The detail of the training and testing process will be performed based on these trajectory data.

4.2. Training and Testing Process of the LSTM Network

The whole dataset is divided into a training set, a verification set, and a test set in the proportion of seven, two, and one. The coefficients related to the training are set as, $lr = 0.001$, $n\_epoch = 2000$ $batch\_size = 200$, $random\_seed = 40$, $timestep = 100$, and $patience = 40$. The variation of loss adopted as the Root Mean Square Error during the training is shown in Figure 7.

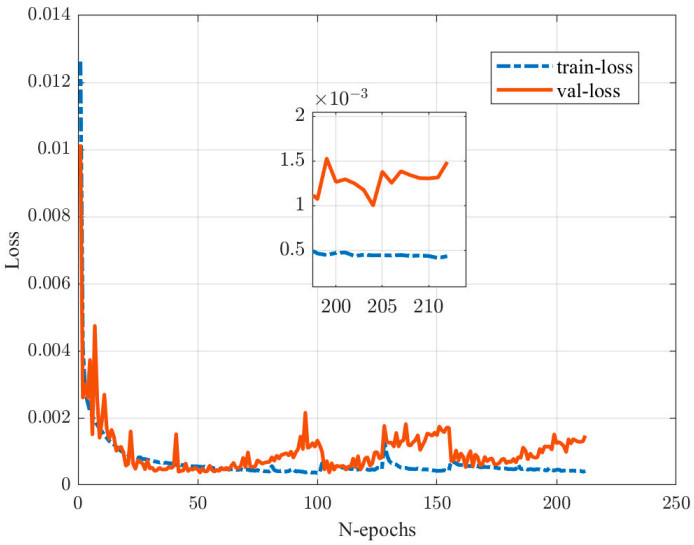

Figure 7. The loss curve during the training process.

From Figure 7, it can be seen that with the increased times of iteration, the loss in the training set and verification set declined rapidly at first, and then the downward trend turned to slow. Finally, the loss in the training set stabilized at 0.5×10^{-3}, while the loss in the verification settles at 1.0×10^{-3} at the 210 *n_epoch*. The expected loss value is satisfied in the training and verification process of the LSTM network.

As the loss value has stayed at a relatively low level, the trained LSTM network is used in the real-time guidance to test the accuracy of the prediction about residual flight time. The prediction results compared with the real time-to-go are shown in Figure 8. The predicted time-to-go of four successive ballistics and the predicted time error are displayed. It can be seen that the predicted time-to-go results based on the LSTM network are similar to the real results, and the time errors deviated by the predicted and real time-to-go are placed within a range of ±10 s. Moreover, the computation time cost of LSTM is, on average, about 10 ms, while the numerical method is generally about 60 ms, which means that the time-to-go solver based on the LSTM network achieves a five-times-higher computation efficiency and can be adopted for online cooperative time guidance.

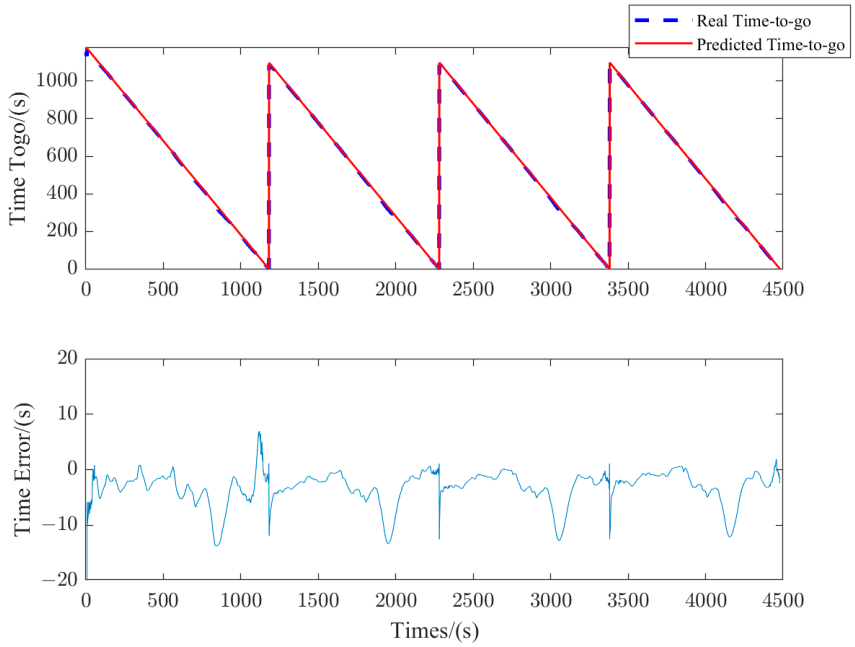

Figure 8. Test results of predicted time-to-go.

4.3. Multiple Vehicles Simulation

In this simulation, the proposed time cooperative guidance based on the modified artificial potential field will be subjected to multiple hypersonic vehicles. The simulation scene contains multiple no-fly zones, whose positions and radii are listed in Table 2. The three vehicles with different initial states could communicate with each other and need to arrive at the same target region at the coordinated time. The initial simulation conditions of the three vehicles are described in Table 3. The flight time range of each vehicle is generated by Monte Carlo simulations in different widths of the heading angle corridor.

Table 2. The different positions and radii of multiple no-fly zones.

No-Fly Zone	1	2	3	4	5	6	7
Position Radius/km	36° E, 2° N 300	26° E, 5° N 275	32.5° E, 11° N 300	44° E, 3.5° N 250	27.8° E, 5.1° N 250	45° E, −5° N 275	40° E, 20° N 250

Table 3. The initial conditions of the time cooperative mission.

Vehicles	Height (km)	Velocity (m/s)	Longitude (°)	Latitude (°)	Flight Path Angle (°)	Heading Angle (°)	Flight Time Range (s)
Vehicle 1	70	7000	0	15	0	90	1222–1400
Vehicle 2	70	7000	0	0	0	90	1212–1389
Vehicle 3	70	7000	0.5	−14	0	80	1312–1522
Terminal constraints	25	1550	55.4	5.5	-	-	-

The results of the time cooperative simulation for three vehicles are shown in Figure 9. Figure 9a,b shows that the three-dimensional and horizontal trajectories for three vehicles. The cylindrical regions with blue surfaces denoted as no-fly zones are all successfully avoided by the three vehicles, which satisfied the constraints (10). It can be seen from Figure 9c that all three longitudinal trajectories are inside the H-V boundaries consisting of heat flow, overload, dynamic pressure, and QEGC condition, which means the constraints (5)–(9) are perfectly met. Figure 9d displays the bank angle profile versus time, and it can be inferred that the reverse times of the bank angle are reasonable, which reduces the burden of the attitude control systems.

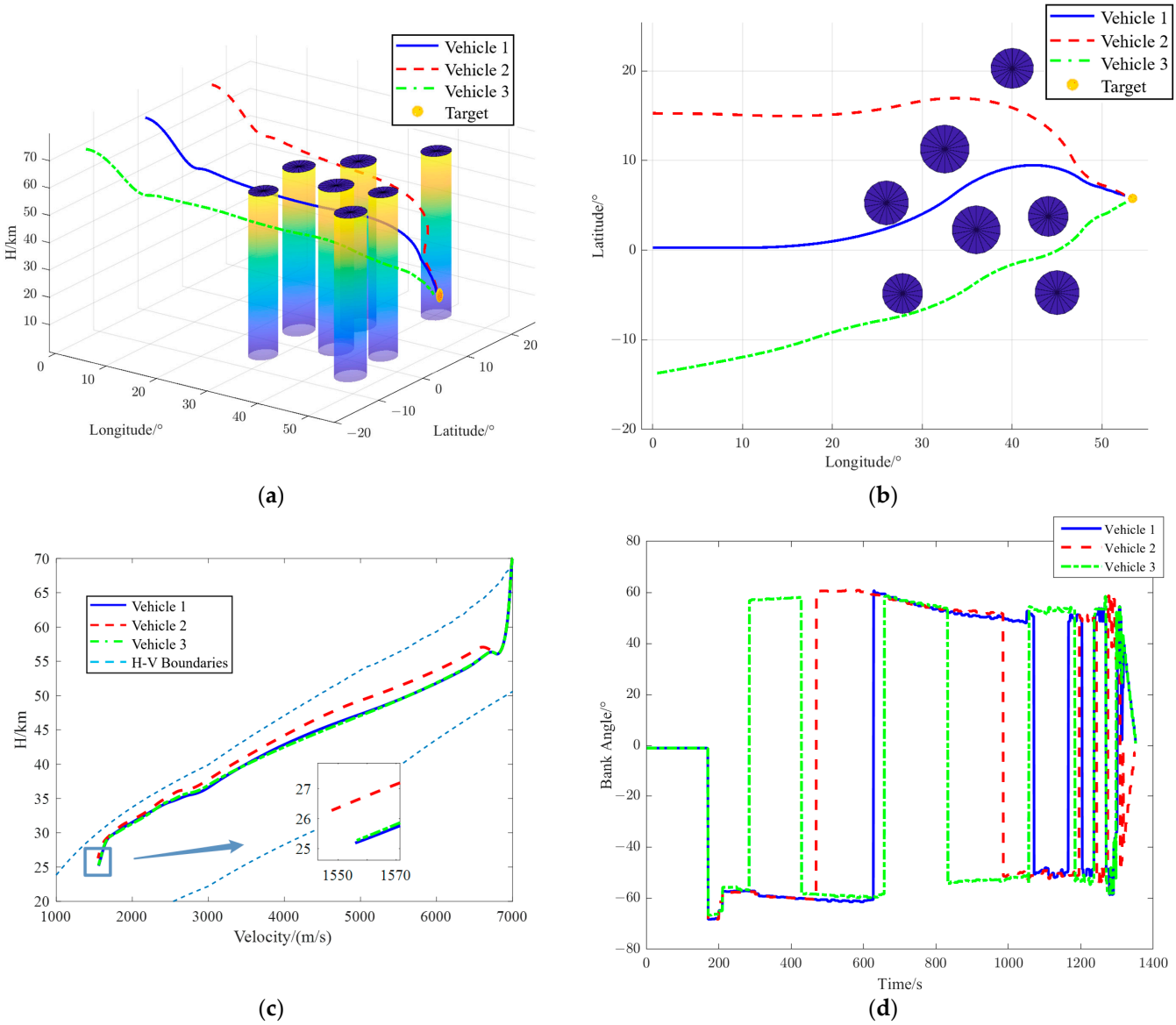

Figure 9. Simulation result of time cooperation. (**a**) The three-dimensional trajectories of three vehicles; (**b**) horizontal trajectories of multiple vehicles in time cooperative guidance simulations; (**c**) longitudinal trajectories of multiple vehicles in time cooperative guidance simulations; (**d**) bank angle profiles of multiple vehicles in time cooperative guidance simulations.

The prediction of the residual flight time of three vehicles during the glide phase is shown in Figure 10. Combined with the flight time range in Table 3, it can be analyzed that the residual flight times of vehicles 1 and 2 are less than vehicle 3 because of the different distances to the target, which leads to a huge time error between the vehicles at the beginning of the glide phase. Afterwards, as the coordinated time generated by the time decision module is delivered to each vehicle, the error of the time-to-go decreases rapidly according to the influence of the time potential field. It can be visually seen in Figure 9b that the horizontal track of vehicle 3 is more straight towards the target, which narrows the flight time, while vehicles 1 and 2 make large-scale maneuvers, which delay the flight times. The three predicted times-to-go converge in a similarly consistent state by the consequence of the time potential field, which drives the three vehicles' arrival at the target region at the coordinated time, 1350 s, and satisfies the constraints (11).

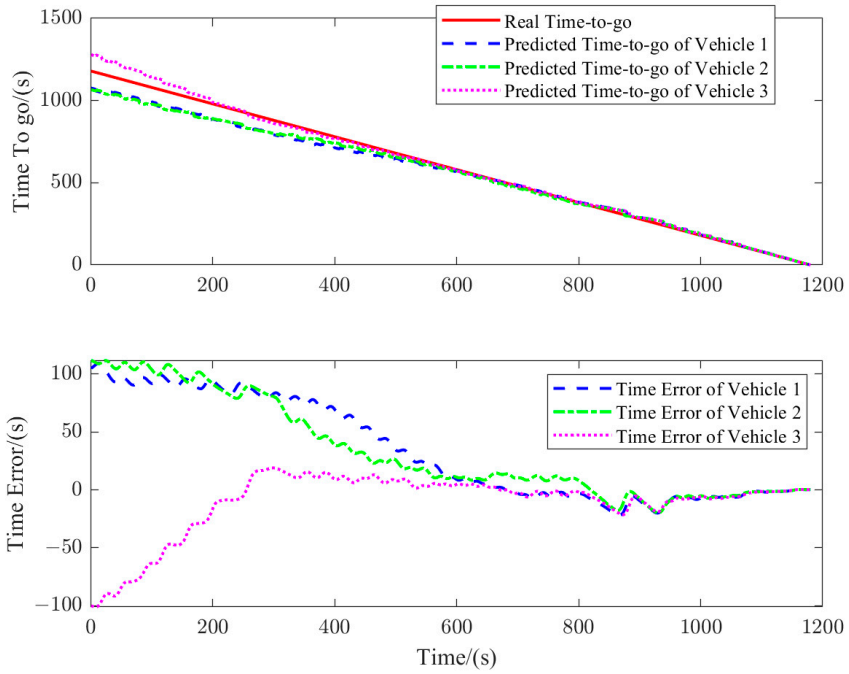

Figure 10. The prediction of residual flight time of the three vehicles.

Furthermore, the other guidance proposed in [23] is compared to test the capability of the time cooperative guidance. The method of article [23] is marked as Law 1, while the algorithm developed in this paper is marked as Law 2. The simulation initial conditions and terminal constraints are the same as Table 3, and the simulation results are shown in Figure 11. The detailed terminal date is given in Table 4.

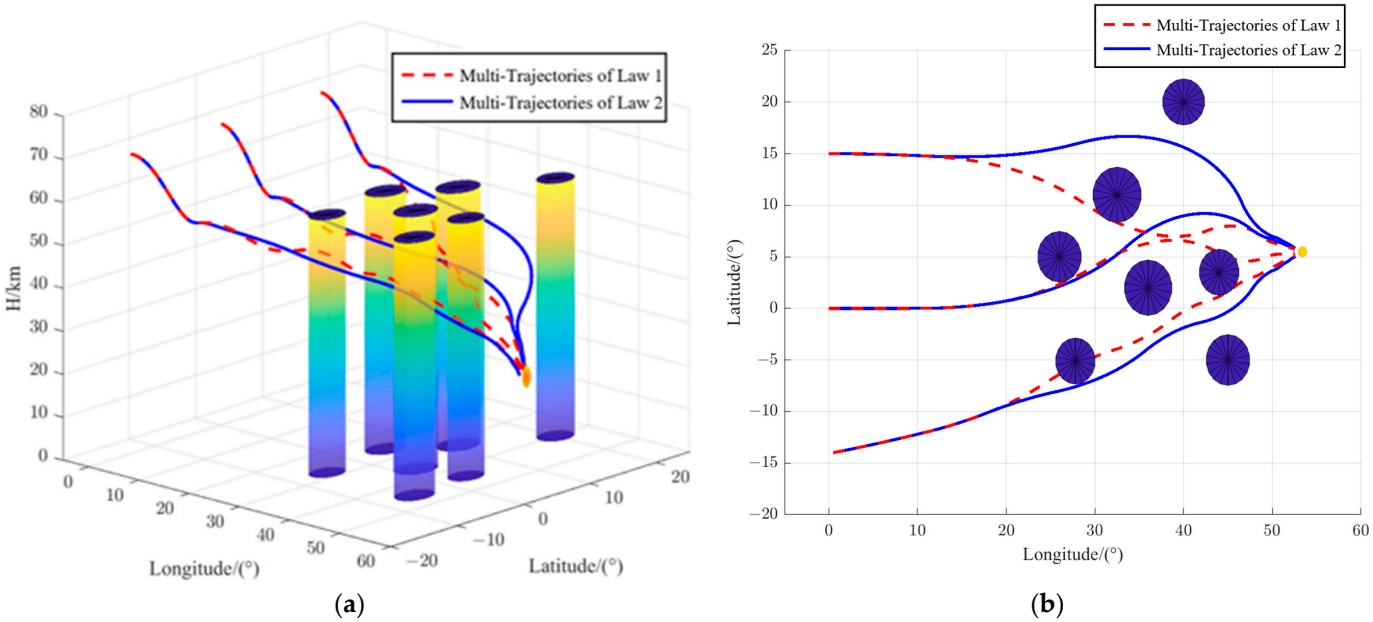

(**a**) (**b**)

Figure 11. Simulation results of time cooperative guidance Law 1 and Law 2. (**a**) The three-dimensional trajectories of three vehicles in Law 1 and Law 2; (**b**) horizontal trajectories of multiple vehicles in Law 1 and Law 2.

Table 4. Terminal states of time cooperative guidance Law 1 and Law 2.

Vehicle	**Vehicle 1**		**Vehicle 2**		**Vehicle 3**	
Guidance Law	Law 1	Law 2	Law 1	Law 2	Law 1	Law 2
Terminal height (km)	25.3	25.2	25.4	25.3	25.2	25.1
Terminal velocity (m/s)	1554.5	1555.2	1552.1	1553.5	1555.0	1555.2
Coordinated time (s)	1325	1350	1325	1350	1325	1350
Actual arrival time (s)	1291	1351	1310	1350	1338	1349
Time error (s)	−34	+1	−15	0	+13	−1

From Figure 11, it can be seen that vehicles 2 and 3 flew thorough the no-fly zone in Law 1, which means that Law 1 only has the ability to adjust the flight time and fails to avoid the no-fly zone constraints. Moreover, the three trajectories of vehicles in Law 2 are smoother than Law 1 in the longitudinal plane, owing to the height feedback control. As described in Table 4, the terminal velocity and height constraints are all satisfied in Law 1 and Law 2; however, the time error in Law 1 is bigger than in Law 2 because of the limited time adjustment ability. The adjusted range of time mentioned in Law 1 is about 0–4%, which is hard to deal with in the time cooperative mission in this simulation. Additionally, the capability of time control in Law 2 proposed in this paper is about 0–12%, which is three times that of Law 1, which can accomplish the mission with a huge initial time error.

5. Conclusions

In this paper, a time cooperative guidance based on the LSTM network and a modified artificial potential field is settled for multiple hypersonic vehicles. The time cooperation framework is firstly designed, whose time prediction solver based on the LSTM network is adopted to estimate the residual flight time online with high accuracy. Additionally, the cooperative time decision module is built to generate the coordinated time by collecting the predicted time-to-go. Additionally, the novel time potential field is then developed in the cooperative time control module to adjust the flight time of multiple hypersonic vehicles and achieve the task of time cooperation, which is well compatible with the typical potential field.

From the simulation results, the main contribution of the time cooperative guidance law proposed in this paper is solving the multiple constraints in time cooperative problems of hypersonic vehicles, especially the no-fly zone and coordination constraints, which are rarely studied by other articles. Additionally, owing to the good performance of the LSTM network, it is possible to design the time cooperative guidance as real-time guidance. Moreover, the ability of time adjustment is enlarged to 12% based on the time potential field, which could be applied in more a complex scene.

Author Contributions: Conceptualization, J.S. and X.X.; methodology, X.X. and X.T.; software, X.X.; validation: X.X. and X.T.; formal analysis, J.S. and X.X.; investigation, X.T. and K.Z.; resources, X.X. and X.T.; data curation, J.S.; writing—original draft preparation, X.X.; writing—review and editing, X.X.; visualization, X.X.; supervision, J.S.; project administration, J.S.; funding acquisition, J.S. All authors have read and agreed to the published version of the manuscript.

Funding: This work was supported by the National Natural Science Foundation of China under Grants 61473015, 91646108 and 62073020.

Data Availability Statement: Not applicable.

Acknowledgments: The authors thank their colleagues for their constructive suggestions and research assistance throughout this study.

Conflicts of Interest: The authors declare no conflict of interest.

References

1. Zhang, Y.Z.; Xu, J.L.; Yao, K.J.; Liu, J.L. A new UAV swarm pursuit task scheme driven by DDPG algorithm. *Acta Aeronaut.* **2020**, *41*, 32–40.
2. Luo, Y.; Song, J.; Zhao, K.; Liu, Y. UAV-Cooperative Penetration Dynamic-Tracking Interceptor Method Based on DDPG. *Appl. Sci.* **2022**, *12*, 1618. [CrossRef]
3. Jeon, I.S.; Lee, J.I.; Tahk, M.J. Homing guidance law for cooperative attack of multiple missiles. *J. Guid. Control Dyn.* **2010**, *33*, 275–280. [CrossRef]
4. Yu, J.L.; Dong, X.W.; Li, Q.D.; Ren, Z.; Lv, J.H. Cooperative guidance strategy for multiple hypersonic gliding vehicles system. *Chin. J. Aeronaut.* **2020**, *33*, 88–96. [CrossRef]
5. Yu, W.; Chen, W.; Jiang, Z.; Zhang, W.; Zhao, P. Analytical entry guidance for coordinated flight with multiple no-fly-zone constraints. *Aerosp. Sci. Technol.* **2018**, *84*, 273–290. [CrossRef]
6. Li, Z.; He, B.; Wang, M.; Lin, H.; An, X. Time-coordination entry guidance for multi-hypersonic vehicles. *Aerosp. Sci. Technol.* **2019**, *89*, 123–135. [CrossRef]
7. Li, Z.; Peng, B.; Li, Z.; Chen, H.; Chen, J. Time-coordinated reentry guidance law for reusable launch vehicle. In Proceedings of the 2019 IEEE International Conference on Unmanned Systems (ICUS), Beijing, China, 7–19 October 2019; IEEE: Beijing, China, 2019.
8. Cong, M.; Cheng, X.; Zhao, Z.; Li, Z. Studies on Multi-Constraints Cooperative Guidance Method Based on Dis-tributed MPC for Multi-Missiles. *Appl. Sci.* **2021**, *11*, 10857. [CrossRef]
9. Wang, L.; Peng, K.; Zhang, W.; Wang, D. Neural Extended State Observer Based Intelligent Integrated Guidance and Control for Hypersonic Flight. *Energies* **2018**, *11*, 2605. [CrossRef]
10. Chai, R.; Tsourdos, A.; Savvaris, A.; Chai, S.; Xia, Y.; Chen, C.P. Six-DOF Spacecraft Optimal Trajectory Planning and Real-Time Attitude Control: A Deep Neural Network-Based Approach. In *IEEE Transactions on Neural Networks and Learning Systems*; IEEE: New York, NY, USA, 2019; pp. 5005–5013.
11. Wang, J.; Wu, Y.; Liu, M.; Yang, M.; Liang, H. A Real-Time Trajectory Optimization Method for Hypersonic Vehicles Based on a Deep Neural Network. *Aerospace* **2022**, *9*, 188. [CrossRef]
12. Sutton, E.S.; Barto, A.G. *Reinforcement Learning: An Introduction*; MIT Press: Cambridge, MA, USA, 2005.
13. Sagliano, M.; Mooij, E. Optimal drag-energy entry guidance via pseudo-spectral convex optimization. *Aerosp. Sci. Technol.* **2021**, *17*, 70–96.
14. Zhao, K.; Song, J.; Luo, Y.; Liu, Y. Research on Game-Playing Agents Based on Deep Reinforcement Learning. *Robotics* **2022**, *11*, 35. [CrossRef]
15. Harpold, J.C.; Graves, C.A., Jr. Shuttle entry guidance. In Proceedings of the 25th Anniversary Conference, Houston, TX, USA, 30 October–2 November 1978; American Astronautical Society: Houston, TX, USA, 1978; Volume 1, p. 35.
16. Liang, Z.; Yu, J.; Ren, Z.; Li, Q. Trajectory planning for cooperative flight of two hypersonic entry vehicles. In Proceedings of the 21st AIAA International Space Planes and Hypersonics Technologies Conference, Xiamen, China, 6–9 March 2017; AIAA: Reston, VA, USA, 2017; p. 2251.
17. Zhang, P.; Zhang, X. Multiple missiles fixed-time cooperative guidance without measuring radial velocity for maneuvering targets interception. *ISA Trans.* **2021**, *126*, 388–397. [CrossRef] [PubMed]
18. He, S.; Wang, W.; Lin, D.; Lei, H. Consensus-based two-stage salvo attack guidance. In *IEEE Transactions on Aero-Space and Electronic Systems*; IEEE: New York, NY, USA, 2018; Volume 54, pp. 1555–1566.
19. Zhao, J.; Zhou, R.; Dong, Z. Three-dimensional cooperative guidance laws against stationary and maneuvering targets. *Chin. J. Aeronaut.* **2015**, *28*, 1104–1120. [CrossRef]
20. Khatib, O. Real time obstacle Avoidance for manipulation and mobile robots. *Int. J. Robot. Res.* **1986**, *5*, 90–98. [CrossRef]
21. Li, Z.; Yang, X.; Sun, X.; Liu, G.; Hu, C. Improved artificial potential field based lateral guidance for waypoints passage and No-fly zones avoidance. *Aerosp. Sci. Technol.* **2019**, *86*, 119–131. [CrossRef]
22. Hu, Y.; Gao, C.; Li, J.; Jing, W.; Chen, W. A novel adaptive lateral reentry guidance algorithm with complex distributed no-fly zones constraints. *Chin. J. Aeronaut.* **2021**, *35*, 128–143. [CrossRef]
23. Fang, K.; Zhang, Q.; Ni, K.; Cheng, L.; Huang, Y. Time-coordinated reentry guidance law for hypersonic vehicle. *Acta Aeronaut. Astronaut. Sin.* **2018**, *39*, 321958.